Impact of fast-solidification on all-d-metal NiCoMnTi based giant magnetocaloric Heusler compounds

Zhang, Fengqi; Wu, Ziying; Wang, Jianlin; Wu, Zhenduo; Zhao, Chenglong; Eijt, Stephan; Schut, Henk; van Dijk, Niels; Brück, Ekkes; More Authors

DOI
10.1016/j.actamat.2023.119595

Publication date
2024

Document Version
Final published version

Published in
Acta Materialia

Acta Materialia 265 (2024) 119595

Contents lists available at ScienceDirect

Acta Materialia

journal homepage: www.elsevier.com/locate/actamat

Full length article

Impact of fast-solidification on all-*d*-metal NiCoMnTi based giant magnetocaloric Heusler compounds

Fengqi Zhang [a,b,**], Ziying Wu [a], Jianlin Wang [c], Wenyu Chen [d], Zhenduo Wu [e,*], Xiang Chi [f], Chenglong Zhao [g], Stephan Eijt [a], Henk Schut [h], Xuedong Bai [c], Yang Ren [b,i,j,*], Niels van Dijk [a], Ekkes Brück [a]

[a] Fundamental Aspects of Materials and Energy (FAME), Faculty of Applied Sciences, Delft University of Technology, Mekelweg 15, Delft 2629JB, The Netherlands
[b] Department of Physics, City University of Hong Kong, Kowloon, Hong Kong
[c] State Key Laboratory for Surface Physics, Institute of Physics, Chinese Academy of Sciences, Beijing, China
[d] Department of Materials Science and Engineering, City University of Hong Kong, Kowloon, Hong Kong
[e] City University of Hong Kong (Dongguan), Dongguan, China
[f] Songshan Lake Materials Laboratory, Dongguan, China
[g] Storage of Electrochemical Energy, Faculty of Applied Sciences, Delft University of Technology, Mekelweg 15, Delft 2629JB, The Netherlands
[h] Neutron and Positron Methods for Materials, Faculty of Applied Sciences, Delft University of Technology, Mekelweg 15, Delft 2629JB, The Netherlands
[i] Shenzhen Research Institute, City University of Hong Kong, Shenzhen 518057, Guangdong, China
[j] Centre for Neutron Scattering, City University of Hong Kong, Kowloon, Hong Kong

ARTICLE INFO

Keywords:
Magnetocaloric effect
All-*d*-metal Heusler compounds
Ni-Co-Mn-Ti
Lattice defects

ABSTRACT

Recently, the all-*d*-metal Ni(Co)MnTi based Heusler compounds are found to have a giant magnetocaloric effect (GMCE) near room temperature and manifest different functionalities like multicaloric effects, which can be employed for solid-state refrigeration. However, in comparison to other traditional Heusler compounds, the relatively large thermal hysteresis (ΔT_{hys}) and moderately steep ferromagnetic phase transition provides limitations for real applications. Here, we present that fast solidification (suction casting) can sufficiently tailor the GMCE performance by modifying the microstructure. Compared with the arc-melted sample, the magnetic entropy change of the suction-casted sample shows a 67% improvement from 18.4 to 29.4 $Jkg^{-1}K^{-1}$ for a field change ($\Delta\mu_0 H$) of 5 T. As the thermal hysteresis has maintained a low ΔT_{hys} value (5.5 K) for the enhanced first-order phase transition, a very competitive reversible magnetic entropy change of 21.8 $Jkg^{-1}K^{-1}$ for $\Delta\mu_0 H = 5$ T is obtained. Combining high-resolution transmission electron microscopy (HRTEM) and positron annihilation spectroscopy (PAS) results, the difference in lattice defect concentration is found to be responsible for the significant improvement in GMCE for the suction-cast sample, which suggests that defect engineering can be applied to control the GMCE. Our study reveals that fast solidification can effectively regulate the magnetocaloric properties of all-*d*-metal NiCoMnTi Heusler compounds without sacrificing ΔT_{hys}.

1. Introduction

Magnetic materials that show a first-order magnetic transition (FOMT) from a disordered to an ordered magnetic state, create a noticeable isothermal entropy change and an adiabatic temperature change (ΔT_{ad}), and are known as giant magnetocaloric effect materials (GMCMs) [1]. These GMCMs can be designed for specific applications like solid-state magnetic refrigeration [2–5], magnetic heat pumps [6] and thermomagnetic generators to covert low-temperature waste heat into electricity [7,8]. Generally, two mechanisms, which are magnetoelastic coupling and magnetostructural coupling, can efficiently give rise to the giant magnetocaloric effect (GMCE). In recent 20 years, several model GMCMs have been found, including $Gd_5(Si_2Ge_2)$ [1], $(Mn,Fe)_2(P,X)$ based compounds (X = As, Ge, Si) [9], $La(Fe,Si)_{13}$ based materials [10], NiMn-X based magnetic Heusler alloys (X = Al, Ga, In, Sn, Sb) [11], MnM-X (M = Co or Ni, X = Si or Ge) ferromagnets [12,13], and FeRh [14]. Within these GMCMs, recently, the unconventional all-*d*-metal Ni(Co)MnTi based Heusler compounds have received significant

** Corresponding author at: Department of Physics, City University of Hong Kong, Kowloon, Hong Kong.
* Corresponding authors.
E-mail addresses: F.Zhang-7@tudelft.nl (F. Zhang), zd.wu@cityu.edu.cn (Z. Wu), yangren@cityu.edu.hk (Y. Ren).

https://doi.org/10.1016/j.actamat.2023.119595
Received 2 June 2023; Received in revised form 7 December 2023; Accepted 10 December 2023
Available online 11 December 2023

attention because of its unique bonding stabilization in the whole system (*d-d* hybridization) [15], its well-tunable GMCE [16–18] and its excellent mechanical properties [19,20] in comparison with traditional NiMn-*X* based magnetic Heusler alloys (*X* = Al, Ga, In, Sn, Sb).

Different optimization strategies have been applied for this all-*d*-metal NiCoMnTi based Heusler system. For example, by optimizing the heat treatment of the normal arc-melting compounds the value of magnetic entropy change (Δs_T), based on the calculation of isofield magnetization data, can reach 38 $Jkg^{-1}K^{-1}$ for $\Delta\mu_0 H = 2$ T [17]. Rapid solidification (melt spinning) can also be used to enhance the GMCE performance in the NiCoMnTi based Heusler system, where Δs_T can reach about 27 $Jkg^{-1}K^{-1}$ for $\Delta\mu_0 H = 2$ T [16]. However, the large changes in microstructure result in an increased ΔT_{hys} of 19 K, which will significantly degrade the performance. This signifies that tuning the solidification conditions by carefully modifying the microstructure can be an efficient way to manage its GMCE. Compared with melt-spinning (with cooling rates above 10^5 K/s), suction casting (with cooling rates of 10^2 K/s) provides a relatively mild modification of the microstructure due to the slower cooling rates (about 100 K/s), and can therefore be used to design different materials microstructures [21]. In the present study, arc-melted and suction-cast $Ni_{37}Co_{13}Mn_{35}Ti_{15}$ compounds have been produced and the thermodynamic, GMCE, microstructural properties have been reported. In comparison with the arc-melted sample, it is found that the suction-cast sample exhibits a sharper FOMT, while a low ΔT_{hys} is maintained at 5.5 K. As a result, a very competitive reversible $\Delta s_T^{MH}$of 21.8 $Jkg^{-1}K^{-1}$ for $\Delta\mu_0 H = 5$ T is obtained for the suction-cast sample from the calculation of isothermal magnetization data in different fields. The responsible mechanism has been investigated from its microstructural aspects. It is found that the favorable properties can result from the reduced concentration in lattice defects, which suggests that defect engineering can be used to control the GMCE in these Heusler compounds. Our current studies elucidate that fast solidification can efficiently regulate the magnetocaloric properties in all-*d*-metal NiCoMnTi Heusler materials.

2. Experimental procedure

High-purity (99.9 %) raw materials are used to prepare polycrystalline samples with a nominal composition of $Ni_{37}Co_{13}Mn_{35}Ti_{15}$ using high-vacuum (< 10^{-6} mbar) arc-melting and suction-casting under Ar atmosphere. The samples are melted for 5 times for good homogeneity. To compensate for evaporation losses of Mn during melting, 4 at.% extra Mn is introduced. Suction rods with 8 mm diameter are cast as SC sample, and the corresponding suction-cast rod is produced out of the arc-melted sample directly. Then the as-cast AM and SC samples were sealed in quartz tubes under Ar atmosphere and annealed for 6 days at 1173 K in a vertical oven [22]. Subsequently, these samples were rapidly quenched from the annealing furnace into cold water, denoted as AM sample and SC sample, respectively.

Zero-field differential scanning calorimetry (DSC) measurements were carried out using a commercial TA-Q2000 DSC calorimeter. X-ray diffraction (XRD) patterns in the high-temperature austenite state (structural phase-transition temperature T_{str} + 100 °C) were collected using an Anton Paar TTK450 temperature chamber and a PANalytical X-pert Pro-diffractometer with Cu K_α radiation. Note that the residual strain inside the materials has been released by annealing the powders at 500 °C for 5 h under Ar atmosphere. The above XRD patterns were analysed using Fullprof's implementation of the Rietveld refinement method [23]. Moreover, the temperature-dependent magnetization (*M-T*) and the field-dependent magnetization (*M-H*) curves for all samples were measured in a superconducting quantum interference device (SQUID, Quantum Design MPMS 5XL) magnetometer. The isothermal *M-H* measurements at different temperatures were performed by the so-called loop method [24]. The samples were initially cooled down to 180 K (complete martensite region) and then subsequently warmed up to the target temperature at a rate of 2 K/min. Doppler broadening positron annihilation spectroscopy (DB-PAS) was employed to study the lattice defects in the samples. DB-PAS depth profiles were measured at room temperature with positron implantation energies ranging from 0.1 to 25 keV, using the variable energy positron beam facility at the Reactor Institute Delft [25]. A high-purity Ge (HPGe) detector cooled by liquid nitrogen with an energy resolution of 1.2 keV at 511 keV was used to detect the energy distribution of the 511 keV γ-rays produced by the annihilation of positrons and electrons. The intensity of the low-energy positron beam at the sample position is about 10^4 e^+/s, and the full width at half maximum (FWHM) of the beam diameter is about 8 mm. The depth profiles of the extracted shape (*S*) and wing (*W*) parameters were fitted by the VEPFIT program [26]. The actual compositions for the AM and SC samples have been determined by scanning electron microscopy (SEM) with energy dispersive X-ray spectroscopy (EDX), as shown in Table S1 (Supplementary Information). The EDX maps in Fig. S1 (Supplementary Information) indicate that there is no obvious phase segregation within the matrix. In addition, the basic morphology of samples was investigated by optical microscopy and SEM (FEI Quanta TM 450 FEG). The TEM specimens were prepared with a focused ion beam system (FIB) using the lift-out method. The HRTEM analysis for these two samples was performed using a JEM-F200 and digital image processing was performed by the DigitalMicrograph software (GMS 3, Gatan Inc).

3. Results and discussion

The heat flow as a function of temperature measured by zero-field DSC for the AM and SC samples is presented in Fig. 1a. Compared with the AM sample, it is observed that the endothermic and exothermic peaks shift to lower temperatures and become sharper for the SC sample, which phenomenologically indicates the first-order phase transition will be sharper. From the DSC results, the corresponding characteristic temperatures (T_M^s, T_M^f, T_M, T_A^s, T_A^f, T_A), the thermal hysteresis ΔT_{hys} and entropy change of the transition (Δs_T^{DSC}) are extracted and summarized in Table 1. The thermal hysteresis is defined as $\Delta T_{hys} = (A_s + A_f - M_s - M_f)/2$ and the entropy change of the transition as $\Delta s_T^{DSC} = \int_{A_s}^{A_f} \frac{1}{T}(Q - Q_{base})\left(\frac{\partial T}{\partial t}\right)^{-1} dT$, where Q is the heat flow and Q_{base} the baseline for the heat flow [27,28]. For these two samples, it is found that ΔT_{hys} is low and $\Delta s_T^{DSC}$is comparable with other good all-*d*-metal NiCoMnTi GMCE materials [18].

Additionally, *M-T* curves are measured in an applied magnetic field of 1 T for the AM and SC samples, as shown in Fig. 1b. A strong FOMT from the low-temperature weak magnetism to high-temperature strong ferromagnetism is observed, with phase transitions located near room temperature. Compared with the AM sample, the transition temperatures of the SC sample were lowered, i.e., $T_{str}^{heating}$ moved from 287.2 to 263.2 K. It is known that in comparison to the traditional arc-melting process, the suction-casting process produced a stronger texture in the grain orientation [29,30]. For NiMn-*X* (*X* = Al, Ga, Sn, In, Sb, Ti) based alloys with a strong magneto-structurally coupled transition, the stress-induced martensitic transition is significantly affected by the texture of the alloy [31]. The orientation relations of the austenite grains formed at high temperature with grain boundaries will determine the amount of martensite formed [32,33]. Meanwhile, the grain refinement by fast solidification (suction-casting) will increase the short-range atomic chemical disorder, which hinders the transition and thereby reduces the martensite start temperature [30]. A similar reduction in the structural transition temperature has been found in Ni-Mn-In intermetallic Heusler compounds for microalloying with boron and Ni-Mn-Ga compounds for nano-structuring [34,35], which is mainly caused by the grain refinement. Additionally, it has been found that T_C of the SC sample decreased simultaneously. The ΔT_{hys} values for the AM and SC

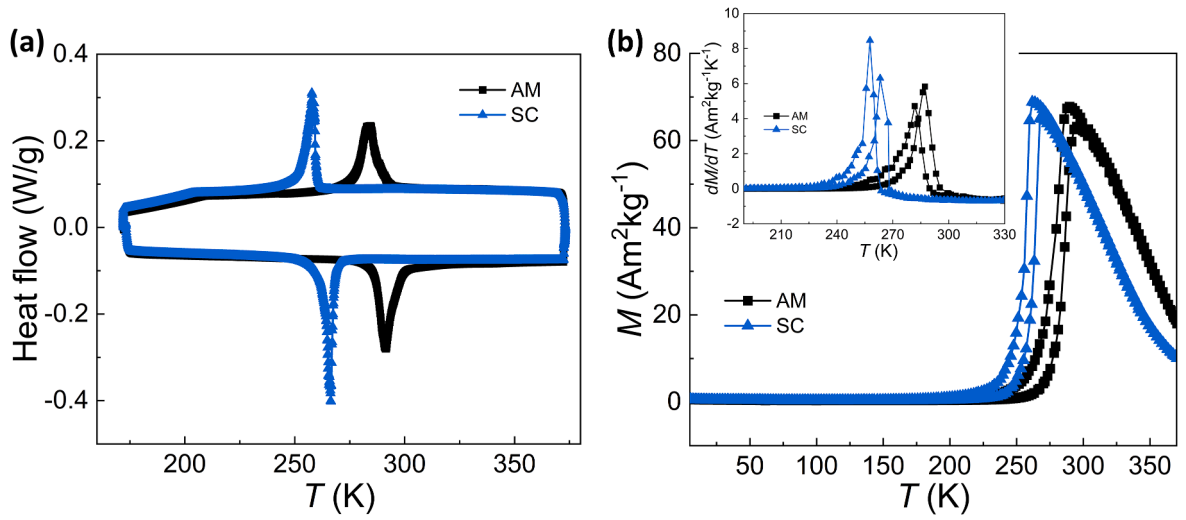

Fig. 1. (a) Heat flow derived from DSC experiments for the AM and SC samples upon warming and cooling processes at a rate of 10 K/min. (b) Iso-field *M-T* curves for the AM and SC samples in a field of 1 T. The inset shows the derived temperature dependence of dM/dT from the *M-T* curves.

Table 1
Summary of the characteristic temperature (T_M^s T_M^f $T_{M,}$ T_A^s T_A^f T_A), the structural temperature upon cooling ($T_{str}^{cooling}$), the structural temperature upon heating ($T_{str}^{heating}$), the thermal hysteresis ΔT_{hys}, the entropy change Δs_T^{DSC}, the change in magnetization ΔM and the field dependence of the transition temperature $dT_{str}/\mu_0 dH$ for the AM and SC samples (measured in DSC and SQUID).

Sample	T_M^s DSC (K)	T_M^f DSC (K)	T_M DSC (K)	T_A^s DSC (K)	T_A^f DSC (K)	T_A DSC (K)	$T_{str}^{cooling}$ SQUID (K)	$T_{str}^{heating}$ SQUID (K)	ΔT_{hys} DSC (K)	ΔT_{hys} SQUID (K)	Δs_T^{DSC} ($Jkg^{-1}K^{-1}$)	ΔM (Am^2kg^{-1})	$dT_{str}/\mu_0 dH$ (K/T)
AM	289.5	276.8	283.2	286.5	295.8	291.2	281.7	287.2	8.0	5.5	36.8	67.8	3.3
SC	260.4	251.3	255.9	260.7	268.6	264.7	257.7	263.2	8.8	5.5	35.3	68.8	3.2

samples by magnetization measurement are only about 5.5 K. These very low ΔT_{hys} values will further contribute to the reversibility of MCE [22,36]. Note that the lower ΔT_{hys} values for the SQUID (2 K/min) in comparison to the DSC (10 K/min) measurements should be ascribed to the slower heating/cooling rates, as shown in Table 1. Because the first-order transitions are driven by nucleation and growth, and the time dependent transitions need certain response time for external fields [37].

To further evaluate the GMCE performance of these two samples, Fig. 2a presents the calculated Δs_T (up to a field change of 0–5 T) as a function of temperature in the vicinity of the martensitic transition. The magnetic entropy changes Δs_T with different magnetic fields $\Delta\mu_0 H$ are calculated based on the Maxwell relation $\Delta s_T(T,\ H) = \int_0^H \left(\frac{\partial M}{\partial T}\right)_H d\mu_0 H$, and the SC sample shows the largest Δs_T peak (for heating) at 29.4 $Jkg^{-1}K^{-1}$ for a field change of $\Delta\mu_0 H = 5$ T. Compared with the AM sample, the maximum value of Δs_T for the SC sample shows a remarkable improvement by 67% from 18.4 to 29.4 $Jkg^{-1}K^{-1}$ for $\Delta\mu_0 H = 5$ T. Considering the application scenarios (using a commercial electromagnet) [38] the reversible part of Δs_T during cycling should be considered. As presented in Fig. 2b, the isothermal magnetic field-cycled *M-H* loops (1st cycle is indicated by the solid symbols and the 2nd cycle by the open symbols) were carefully collected in the temperature range from 251 to 263 K. It is observed that the *M-H* curves do not overlap with each other during the 1st increase and 2nd decrease of the magnetic field cycles. This could result from the presence of some residual austenite that does not contribute to the transformation during the field cycles. This effect has been observed before in the same material system [22]. However, after 2nd cycle no residual phases are observed, thus cycling is reversible [22]. Therefore, the so-called transformation fraction (TF_MH) method is applied assuming that the total magnetization originates from the ferromagnetic austenite phase fraction [36,39]. Consequently, the reversible Δs_T^{MH}($\Delta s_T^{MH\_rev}$) can be determined by combining Eqs. (1) and (2):

$$f_{aus}(T,H) = \frac{M(H) - M_m(H)}{M_a(H) - M_m(H)} \tag{1}$$

$$\Delta s_T^{MH\_rev} = \Delta f \Delta s_T^{DSC} = \left(f(T,H_f) - f(T,H_i)\right)\Delta s_T^{DSC} \tag{2}$$

where $f_{aus}(T,H)$ is the austenite fraction at certain temperature and field, $M(H)$ is the measured magnetization of the sample, and $M_m(H)$ is the magnetization of pure martensite (see the extrapolated black dotted lines in Fig. 2b), $M_a(H)$ is the magnetization of pure austenite, Δs_T^{DSC}refers to the entropy change of the transition derived from DSC (see Table 1), Δf is the transformed austenite fraction. About the difference between Δs_T^{MH} and Δs_T^{DSC}, in general, the Δs_T^{MH} is calculated from the field-dependent magnetization measurements (isothermal protocol), whereas the $\Delta s_T^{DSC}$is from the DSC measurements and represents the entropy change of the full and complete phase transition. Note that the 2nd *M-H* cycle at 263 K is chosen as the reference for pure austenite to avoid an underestimation of the austenite fraction at low fields [22]. For the SC sample the corresponding f_{aus} of the 2nd field cycle at different constant temperatures have been derived, as demonstrated in Fig. 2c. Because of the rapid change in magnetization at low fields, the magnetization values below 1 T (shadow area in Fig. 2c) are excluded to guarantee the validity of data [40,41]. As shown in Fig. 2d, the sharper FOMT and the low ΔT_{hys}, results in a maximum reversible $\Delta s_T^{MH}$for the SC sample of 21.8 $Jkg^{-1}K^{-1}$ at 256 K for $\Delta\mu_0 H = 5$ T. This value is in good agreement with the data (marked as "◆") extracted from the overlap region where the Δs_T determined on cooling and heating are crossing, which therefore corresponds to the reversible Δs_T [28,42,43]. This excellent maximum $\Delta s_T^{MH_rev}$value (21.8 $Jkg^{-1}K^{-1}$) for $\Delta\mu_0 H = 5$ T is

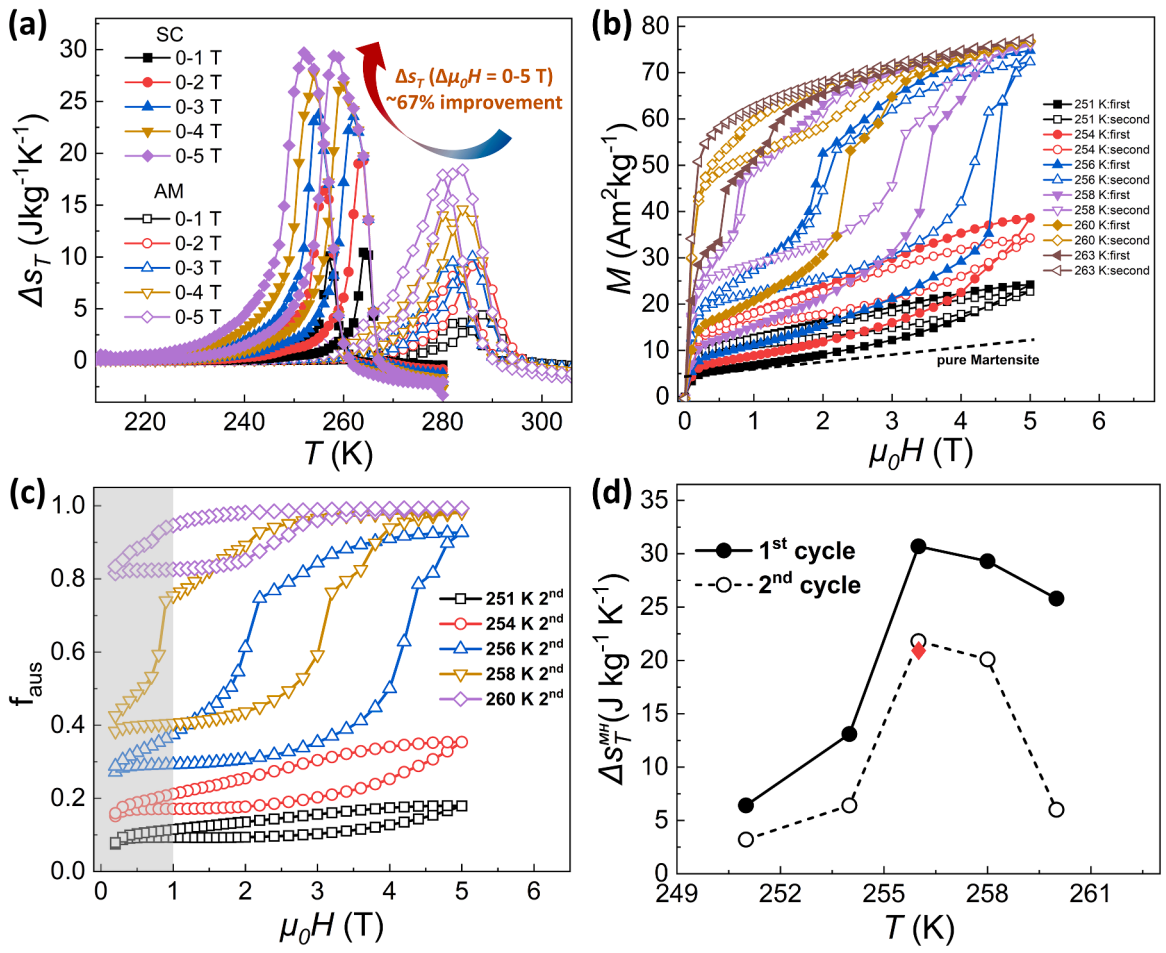

Fig. 2. (a) Magnetic entropy change Δs_T of the AM and SC samples as a function of temperature for both heating and cooling determined for field changes $\Delta\mu_0$H ranging from 1 to 5 T. (b) Iso-thermal *M-H* curves for the SC sample measured during the 1st (solid symbols) and 2nd (open symbols) cycle at different temperatures. The black dotted lines denote the extrapolated magnetization for pure martensite at low temperature. (c) Fraction of austenite f_{aus} for the 2nd cycle at different constant temperatures determined from (b). (d) Δs_T^{MH} for $\Delta\mu_0 H = 5$ T obtained from the TF_MH method during the 1st and 2nd cycles. In the 2nd cycle Δs_T^{MH} is reversible. The red point ("◆") is from the overlap between cooling and heating curves ($\Delta\mu_0 H = 5$ T).

competitive with other NiMn-based Heusler alloys like $Ni_{49.8}Co_{1.2}Mn_{33.5}In_{15.5}$ (14.6 $Jkg^{-1}K^{-1}$) [44], $Ni_{41}Ti_1Co_9Mn_{39}Sn_{10}$ (18.7 $Jkg^{-1}K^{-1}$) [36], $Ni_{48.1}Co_{2.9}Mn_{35.0}In_{14.0}$ (12.8 $Jkg^{-1}K^{-1}$) [40], $Ni_{43}Co_6Mn_{40}Sn_{11}$ (19.3 $Jkg^{-1}K^{-1}$) [39], $Ni_{46}Co_3Mn_{35}Cu_2In_{14}$ (16.4 $Jkg^{-1}K^{-1}$) [45] and $Ni_{36.5}Co_{13.5}Mn_{35}Ti_{15}B_{0.4}$ (18.9 $Jkg^{-1}K^{-1}$) [22]. It can be noted that the peak of Δs_T for the first cycle obtained from the Maxwell relation and TF_MH methods is in good agreement with each other, as found in previous studies [36,41]. And it is worth mentioning that compared with the 1st *M-H* cycle the value of Δs_T^{MH} is obviously degraded from 30.7 to 21.8 $Jkg^{-1}K^{-1}$, which corresponds to a 29% decrease even though the sample has a very low ΔT_{hys} (5.5 K). For samples that show a strong FOMT, it is important to further investigate the reversibility of the MCE, as this defines their potential in real applications [36,41,46–48]. By applying the equation $\Delta T_{ad} = \frac{-T}{C_p}\Delta s_T$, where C_p is the specific heat at certain temperature, the reversible adiabatic temperature change $|\Delta T_{ad}|$ for the SC sample is estimated at 10.7 K for $\Delta\mu_0 H = 5$ T.

To better understand the transformation mechanism, the microstructures for the AM and SC samples have been obtained, as shown in Fig. 3. The HRTEM image in Fig. 3a exhibits the highly ordered austenite area, as there is no obvious lath-like microstructure observed, that is characteristic for the martensite phase [15]. In Fig. 3b the corresponding fast Fourier transform (FFT) for the selected region in Fig. 3a demonstrates its face-centered cubic austenitic structure (*Fm*-3 m; space group 225). The main crystal planes have been indexed successfully. By applying the inverse fast Fourier transform (IFFT) it is found in Fig. 3c, that abundant dislocations are distributed within the main matrix, which might be introduced by the solidification and casting processes. The high density of lattice defects, such as these random dislocations, may influence the development of internal stresses during the martensitic phase transition [49,50]. Moreover, from Fig. 3d the atomic vacancies and vacancy-cluster defects have directly been observed. Edge dislocations are located at the periphery of these point defects. It has been proposed that such quenched-in vacancies through the interaction of clustered vacancies with partial dislocations can prevent the nucleation of martensite [51]. This might be the reason that for almost the complete NiCoMnTi series of compounds made by arc-melting with quenching [20,52–57] (without optimized heat-treatment) the transition cannot easily be tuned towards a sharp transition, compared with other traditional NiMn-*X* (*X* = Al, Ga, In, Sn, Sb) Heusler compounds. However, only fast solidification [16] or higher annealing temperatures [17] can sufficiently regulate the magneto-structurally coupled transition in this materials family. Here we find that this is correlated with the formation and control of lattice defects.

As mentioned before the expected grain refinement is clearly observed for the SC sample, as shown in Fig. 3e. In comparison to the regular arc-melting technique where a cooling rate of about 10 K/s is achieved [29,58], for suction casting [29] and melt spinning [59,60] cooling rates of 10^2 and 10^5 K/s are achieved, respectively. It is found that melt spinning can drastically reduce the grain size down to below 1

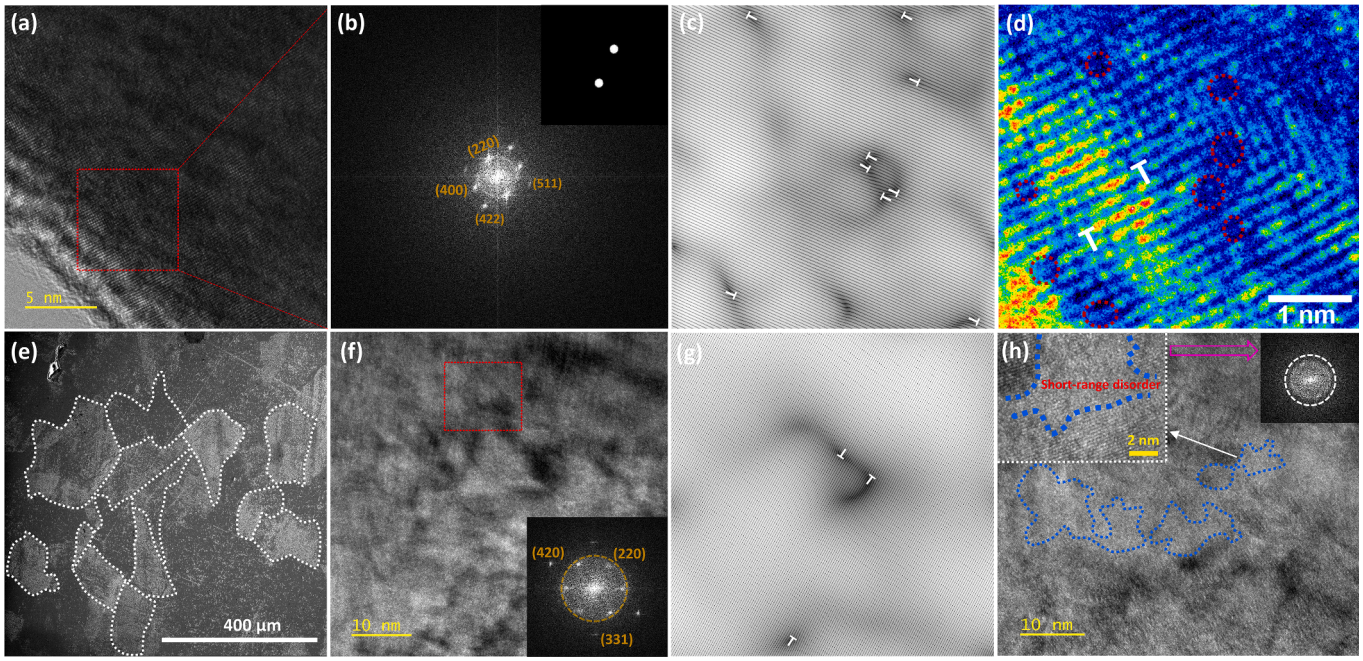

Fig. 3. (a) HRTEM image for the AM sample. (b) Corresponding FFT patterns in the regions indicated by the red box in (a) for the AM sample. The inset is the selected diffraction spots for IFFT. (c) Corresponding IFFT pattern of (b) consisting of numerous dislocations marked with "T" along the (422) direction. (d) False-color image of the partial enlarged HRTEM image from the red region in (a). (e) SEM image of the SC sample showing the grain structure. (f) HRTEM image for the SC sample. The inset is the corresponding FFT pattern in the regions indicated by the red box. (g) Corresponding IFFT pattern of (f) consisting of less dislocations marked with "T" along the (420) direction. (h) HRTEM image for the SC sample. The blue circled area shows short-range disordered lattice: (left) partial enlarged image; (right) FFT patterns for the selected disorder region.

μm [16,61,62]. However, at the same time ΔT_{hys} is increased to 19 K, which is not beneficial for the reversibility [16]. In contrast, the moderate cooling speed for suction casting provides a more gentle modification of the microstructure. As exhibited in Fig. 3e, the average grain size for the SC sample is about 86 μm. Simultaneously, a clear difference can be seen between the AM and the SC sample, as shown in Fig. 4. Optical microscopy shows that the average grain size undergoes a reduction of about a factor 5 from about 370 μm (AM) to about 80 μm (SC). The above findings suggest that by well controlling the microstructure the suction casting with its lower cooling rate can achieves a better GMCE performance with maintaining a low ΔT_{hys}. The electron diffraction in Fig. 3f proves that the cubic austenite phase has been retained after suction casting. Interestingly, compared with the arc-melted sample, a lower concentration of lattice dislocations is found

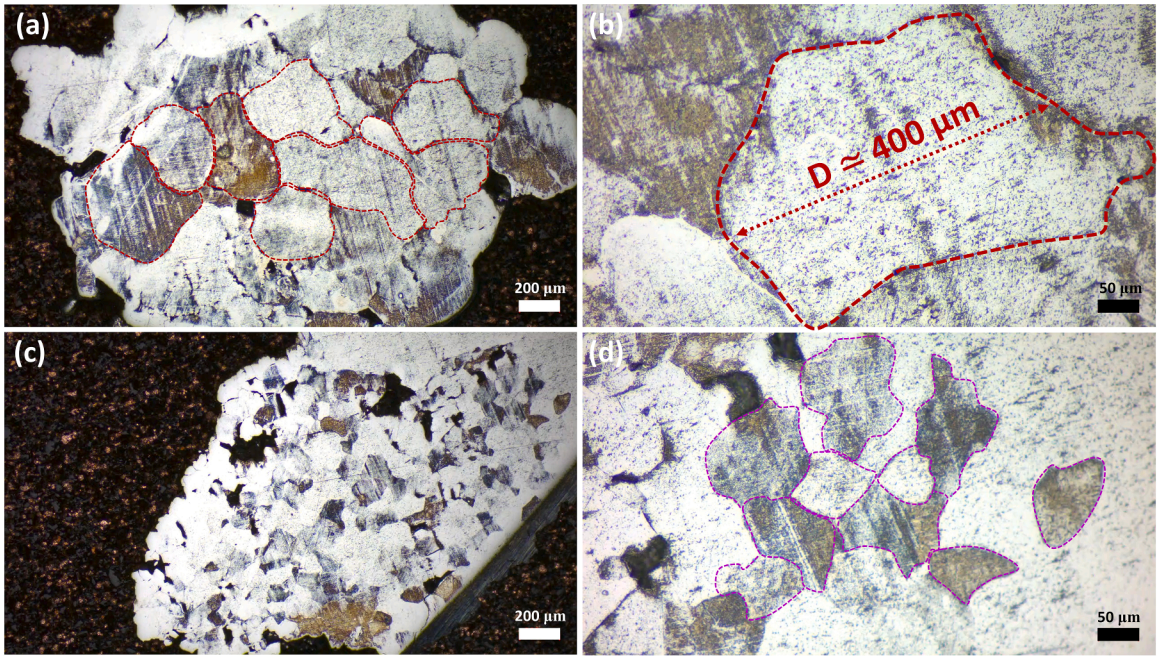

Fig. 4. (a)-(b) Optical microscope images for the etched AM sample. (c)-(d) Optical microscope images for the etched SC sample. The average diameter of grain is about 370 and 80 μm for the AM and SC sample, respectively.

for the SC sample in Fig. 3g. This phenomenon may be closely related to the refined microstructure of the SC sample because a finer grain structure provides more grain boundaries in comparison with the regular coarse microstructure. According to the model proposed by Grabski et al. [63], the grain boundaries can act as sinks for dislocations. This means that the existing dislocations can be incorporated in the grain boundaries by the formation of grain-boundary defects. High-temperature annealing helps the release of strain energy carried by the dislocations [64,65], which accumulates during casting. Once dislocation movement occurs, individual dislocations will interact with neighboring ones, which results in coalescence and annihilations of dislocations at grain boundaries. These processes are diffusion limited and will be influenced by diffusion length and the pinning/trapping with other types of defects. For example, in pure Ni and α-Fe systems it is found that an edge dislocation will strongly interact with vacancies (pipe diffusion) [66]. Hence, it is believed that the higher concentration of vacancies and longer diffusion length for AM sample conduct more dislocations than SC sample. For AM and SC samples, the defect concentrations during heat-treatment are different because of the change in crystallite size resulted from different solidification rates. In addition, it is known that one of the most important functions for fast-quenching treatments is the retention of phases stable at high annealing temperatures [67]. And it also can be used for maintaining the high-temperature vacancy-type point defects (so-called quenched-in vacancies). For example, in specific cases such as in engineering structural materials, there will be a tendency that the vacancies can coalesce into vacancy clusters, and some clusters collapse into dislocation loops which can grow by absorbing more vacancies [68,69]. The fast-quenching process can preserve the dislocations at room temperature in crystal materials, as experimentally observed before [70]. As shown in Fig. 3h some short-range disordered nanostructures (with a diameter of about 10 nm) are distributed within the crystal matrix. The inset (right) is the relevant FFT result, which proves the disordered structure. Abundant disordered structures will be introduced during the suction-casting or other rapid solidification process [71]. Surprisingly, annealing at high temperature (1173 K) did not result in a complete crystallization of these disordered structures. When the annealing temperature is above $0.5T_m$, where T_m is the melting point (around 1380 K for the current samples) [17], it is expected that recrystallization will occur smoothly [72–74]. Actually, the recrystallization can be considered to be a nucleation and growth phenomenon, which is controlled by thermally activated processes [75]. It is known that the process of nucleation and growth will be greatly influenced by lattice defects, for example, non-equilibrium defects such as excess vacancies and dislocations can be recognized as suitable nucleation sites for the heterogeneous nucleation of crystals [68]. From above experimental results, compared with the AM sample, the SC sample contains lower concentrations of vacancies and dislocation defects, which will further inhibit the nucleation and growth processes of recrystallization. In addition, even grain boundaries are also favored sites for nucleation, however, compared with the nanoscale disordered region, the large crystallite size (~86 μm) of the SC sample provides fewer nucleation sites. This will lead to a lower nucleation rate, and the recrystallization becomes slower [75]. Therefore, even at relatively high annealing temperature ($T \simeq 0.8T_m$) the recrystallization of limited amount of disordered structures are still maintained. For instance, similar nano-disordered structures have been noticed in the high-temperature annealed melt-spun ribbons [76]. Interestingly, it is also found that the nano-disordered structures within specific nanocrystal matrix (e.g. Al-Mg alloys) can have robust stability up to melting temperatures [77]. The degree of atomic ordering is found to correlate with the shift in transition temperature for Heusler compounds [49, 78–80]. Furthermore, according to theoretical calculations the T_C of austenite shows a strong correlation with the electron-to-atom ratio (e/a) in the NiCoMnTi system [17]. The e/a was calculated from the actual chemical formula of the compound and it is equal to the concentration weighted sum of the number of 3d and 4 s electrons of Ni ($3d^8 4s^2$), Co ($3d^7 4s^2$), Mn ($3d^5 4s^2$) and Ti ($3d^2 4s^2$) [81]. For the AM and SC samples, the e/a values are calculated as 7.908 and 7.910, respectively, which are almost the same. In other words, the significant changes of transition temperature should mainly be attributed to changes of microstructures between the AM and SC samples rather than the electronic properties. Additionally, it is known that rapid solidification like melt-spinning can introduce disordered structures and a lower ordering which can further decrease transformation and Curie temperature, which had been observed before [78,82]. With regard to the magnetic properties, it is worth mentioning that these disordered structures did not present a magnetic transition at low temperature, as shown in Fig. S2 (Supplementary Information). This is different compared to the reentrant spin-glass type transition found in other Heusler materials [83–85]. Note that at room temperature in the HRTEM the martensite phases co-exist, which indicates that some residual phases exist, as presented in Fig. S3 (Supplementary Information).

To understand the lattice defects from a microscopic perspective, positron annihilation spectroscopy (PAS) is employed for the AM and SC samples. It is well-known that PAS is a non-destructive method and can efficiently obtain information of open-volume defects, such as dislocations and vacancies with a high sensitivity due to the strong affinity between positrons and defects resulting in a positron-electron pair annihilation process [86–89]. As shown in Fig. S4 (Supplementary Information), XRD results suggest that these two samples have a high purity. In Fig. 5, the Doppler broadening characterized by the S and W

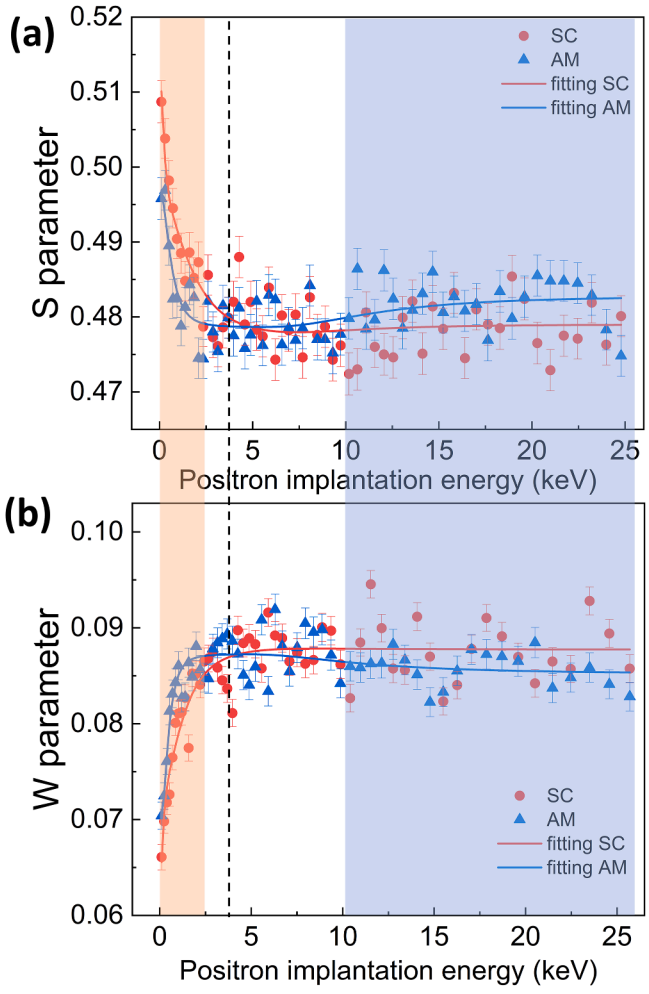

Fig. 5. (a) S parameter and (b) W parameter as a function of the positron implantation energy extracted from positron Doppler broadening (DB) depth profiles for the AM (blue) and the SC (red) sample.

parameters is presented for these two samples as a function of the positron implantation energy (probing the depth profiles). The *S* parameter represents the positron annihilation with valence electrons, which is sensitive to the electronic structure and open-volume defects. The *W* parameter reflects the positron annihilation with (semi-)core electrons, which is responsible for the local chemical environment of the positron trapping sites [90]. As shown in Fig. 5a (orange area), the *S* parameter of the AM and SC samples rapidly decreased in the low energy range up to about 2.5 keV, corresponding to a mean positron implantation depth less than 20 nm. The observed decrease in *S* (increase in *W*) is ascribed to epi-thermal positron remission and positrons annihilating at the surface. When the energy is above 10 keV, the region indicated in blue in Fig 5, a plateau in the *S* and *W* parameters is reached, where positrons are primarily stopped and annihilated in the bulk matrix, at positron mean implantation depths greater than 200 nm. The greater increase in *S* and decrease in *W* for the AM sample means that there are more open-volume lattice defects, such as dislocations and vacancies distributed in the matrix. This is in good agreement with the HRTEM observations in Fig. 3. Combined with the HRTEM data the above PAS results suggest that the presence of lattice defects significantly influences the thermodynamics and kinetics of the strong first-order phase transition in these materials [91]. As a consequence, the transition in the SC sample is sharper in the NiCoMnTi Heusler compounds. Similarly, in NiTi shape memory alloys driven by a martensitic transition it is found by molecular dynamics simulations that defects like vacancies and vacancy clusters have a pronounced effect on the inhibition of the transition [92]. This means that controlling the defect concentration provides a way to control the strong magneto-structurally coupled transition in magnetic Heusler compounds.

4. Conclusions

In summary, arc-melted and suction-cast $Ni_{37}Co_{13}Mn_{35}Ti_{15}$ compounds have successfully been synthesized, and their basic thermodynamic, magnetic and microstructural properties have been investigated utilizing DSC, SQUID, HRTEM and PAS. Compared with the AM sample, it is found that fast solidification (suction casting) can significantly increase Δs_T as the FOMT is enhanced while ΔT_{hys} remained low. Combining the HRTEM and the PAS measurements, the positive enhancement of the GMCE for the SC sample could be attributed to the lower concentration of lattice defects in comparison to the AM sample. Interestingly, the grain refinement and the short-range disorder in the nanostructures could result in a decrease of the transition temperature for the SC sample. Due to the low ΔT_{hys} and the well-tuned FOMT, a good reversibility of the GMCE has been found for the SC sample, resulting in a very competitive reversible Δs_T^{MH} of 21.8 $Jkg^{-1}K^{-1}$ for $\Delta\mu_0 H = 5$ T. Our present results indicate that the fast solidification can efficiently tailor the GMCE properties of these all-*d*-metal NiCoMnTi Heusler compounds by a modification of the structure and lattice defects, which enhances the prospects for future applications.

Declaration of Competing Interest

The authors declare that they have no known competing financial interests or personal relationships that could have appeared to influence the work reported in this paper.

Acknowledgments

The authors thank Anton Lefering, Bert Zwart, Robert Dankelman and Michel Steenvoorden for their technical assistance. F.Q. Zhang greatly appreciates the kind help from Dr. Y.K. Huang (Van der Waals-Zeeman Institute, University of Amsterdam) and Dr. H.Y. Chen (University of Science and Technology Beijing) for sample preparation (vacuum suction casting). This work was supported by the open research fund of Songshan Lake Materials Laboratory (2022SLABFN19) and by NWO in the domain of the Applied and Engineering Sciences (AES) program. F.Q. Zhang and Y. Ren acknowledge financial support from City University of Hong Kong (Project No. 9610533).

Supplementary materials

Supplementary material associated with this article can be found, in the online version, at doi:10.1016/j.actamat.2023.119595.

References

[1] V.K. Pecharsky, K.A. Gschneidner, Giant magnetocaloric effect in Gd5(Si_2Ge_2), Phys. Rev. Lett. 78 (1997) 4494–4497.
[2] E. Brück, Developments in magnetocaloric refrigeration, J Phys. D. Appl. Phys. 38 (2005) R381–R391.
[3] V. Franco, J.S. Blazquez, J.J. Ipus, J.Y. Law, L.M. Moreno-Ramirez, A. Conde, Magnetocaloric effect: from materials research to refrigeration devices, Prog. Mater Sci. 93 (2018) 112–232.
[4] X. Moya, N.D. Mathur, Caloric materials for cooling and heating, Science 370 (2020) 797–803.
[5] A. Kitanovski, Energy applications of magnetocaloric materials, Adv. Energy Mater. 10 (2020), 1903741.
[6] H. Johra, K. Filonenko, P. Heiselberg, C. Veje, S. Dall'Olio, K. Engelbrecht, C. Bahl, Integration of a magnetocaloric heat pump in an energy flexible residential building, Renew. Energ. 136 (2019) 115–126.
[7] T. Christiaanse, E. Brück, Proof-of-concept static thermomagnetic generator experimental device, Metall. Mater. Trans. E 1 (2014) 36–40.
[8] A. Waske, D. Dzekan, K. Sellschopp, D. Berger, A. Stork, K. Nielsch, S. Fähler, Energy harvesting near room temperature using a thermomagnetic generator with a pretzel-like magnetic flux topology, Nat. Energy 4 (2019) 68–74.
[9] O. Tegus, E. Brück, K.H.J. Buschow, F.R. de Boer, Transition-metal-based magnetic refrigerants for room-temperature applications, Nature 415 (2002) 150–152.
[10] F.X. Hu, B.G. Shen, J.R. Sun, Z.H. Cheng, G.H. Rao, X.X. Zhang, Influence of negative lattice expansion and metamagnetic transition on magnetic entropy change in the compound $LaFe_{11.4}Si_{1.6}$, Appl. Phys. Lett. 78 (2001) 3675–3677.
[11] A. Planes, L. Manosa, M. Acet, Magnetocaloric effect and its relation to shape-memory properties in ferromagnetic Heusler alloys, J. Phys. Condens. Mat. 21 (2009), 233201.
[12] N.T. Trung, L. Zhang, L. Caron, K.H.J. Buschow, E. Brück, Giant magnetocaloric effects by tailoring the phase transitions, Appl. Phys. Lett. 96 (2010), 172504.
[13] E.K. Liu, W.H. Wang, L. Feng, W. Zhu, G.J. Li, J.L. Chen, H.W. Zhang, G.H. Wu, C. B. Jiang, H.B. Xu, F.R. de Boer, Stable magnetostructural coupling with tunable magnetoresponsive effects in hexagonal ferromagnets, Nat. Commun. 3 (2012) 873.
[14] M.P. Annaorazov, K.A. Asatryan, G. Myalikgulyev, S.A. Nikitin, A.M. Tishin, A. L. Tyurin, Alloys of the Fe-Rh system as a new class of working material for magnetic refrigerators, Cryogenics 32 (1992) 867–872 (Guildf).
[15] Z.Y. Wei, E.K. Liu, J.H. Chen, Y. Li, G.D. Liu, H.Z. Luo, X.K. Xi, H.W. Zhang, W. H. Wang, G.H. Wu, Realization of multifunctional shape-memory ferromagnets in all-d-metal Heusler phases, Appl. Phys. Lett. 107 (2015), 022406.
[16] H.N. Bez, A.K. Pathak, A. Biswas, N. Zarkevich, V. Balema, Y. Mudryk, D. D. Johnson, V.K. Pecharsky, Giant enhancement of the magnetocaloric response in Ni-Co-Mn-Ti by rapid solidification, Acta Mater. 173 (2019) 225–230.
[17] A. Taubel, B. Beckmann, L. Pfeuffer, N. Fortunato, F. Scheibel, S. Ener, T. Gottschall, K.P. Skokov, H.R. Zhang, O. Gutfleisch, Tailoring magnetocaloric effect in all-d-metal Ni-Co-Mn-Ti Heusler alloys: a combined experimental and theoretical study, Acta Mater. 201 (2020) 425–434.
[18] B. Beckmann, D. Koch, L. Pfeuffer, T. Gottschall, A. Taubel, E. Adabifiroozjaei, O. N. Miroshkina, S. Riegg, T. Niehoff, N.A. Kani, M.E. Gruner, L. Molina-Luna, K. P. Skokov, O. Gutfleisch, Dissipation losses limiting first-order phase transition materials in cryogenic caloric cooling: a case study on all-d-metal Ni(-Co)-Mn-Ti Heusler alloys, Acta Mater. 246 (2023), 118695.
[19] Z.Y. Wei, E.K. Liu, Y. Li, X.L. Han, Z.W. Du, H.Z. Luo, G.D. Liu, X.K. Xi, H.W. Zhang, W.H. Wang, G.H. Wu, Magnetostructural martensitic transformations with large volume changes and magneto-strains in all-d-metal Heusler alloys, Appl. Phys. Lett. 109 (2016), 071904.
[20] Z.Q. Guan, J. Bai, Y. Zhang, J.L. Gu, X.Z. Liang, Y.D. Zhang, L.D. Esling, X. Zhao, L. Zuo, Simultaneously realized large low-temperature magnetocaloric effect and good mechanical properties in $Ni_3{}_6Co_{13}Mn_{35}Ti_{16}$ alloy, J. Appl. Phys. 131 (2022), 165107.
[21] J.J. Wall, C. Fan, P.K. Liaw, C.T. Liu, H. Choo, A combined drop/suction-casting machine for the manufacture of bulk-metallic-glass materials, Rev. Sci. Instrum. 77 (2006), 033902.
[22] F.Q. Zhang, I. Batashev, N. van Dijk, E. Brück, Reduced hysteresis and enhanced giant magnetocaloric effect in B-doped all-d-metal Ni-Co-Mn-Ti-based Heusler materials, Phys. Rev. Appl. 17 (2022), 054032.
[23] H.M. Rietveld, A profile refinement method for nuclear and magnetic structures, J. Appl. Crystallogr. 2 (1969) 65–71.
[24] L. Caron, Z.Q. Ou, T.T. Nguyen, D.T.C. Thanh, O. Tegus, E. Brück, On the determination of the magnetic entropy change in materials with first-order transitions, J. Magn. Magn. Mater. 321 (2009) 3559–3566.

[25] H. Schut, A Variable Energy Positron Beam Facility With Applications in Materials Science, Delft University of Technology, 1990. Ph.D. thesis.
[26] A. Vanveen, H. Schut, J. Devries, R.A. Hakvoort, M.R. Ijpma, Analysis of positron profiling data by means of "VEPFIT", AIP Conf. Proc. 218 (1990) 171–196.
[27] B.D. Ingale, Y.K. Kuo, S. Ram, Phase transformation, microstructure and magnetocaloric properties in polycrystalline bulk Ni50Mn50-zSnz alloys, IEEE T. Magn. 47 (2011) 3395–3398.
[28] J. Liu, X.M. You, B.W. Huang, I. Batashev, M. Maschek, Y.Y. Gong, X.F. Miao, F. Xu, N. van Dijk, E. Brück, Reversible low-field magnetocaloric effect in Ni-Mn-In-based Heusler alloys, Phys. Rev. Mater. 3 (2019), 084409.
[29] P. Diko, V. Kavečanský, S. Piovarči, T. Ryba, Z. Vargova, R. Varga, Microstructure of the NiMnGa heusler alloys prepared by suction casting and melt-spinning, Mater. Sci. Forum (2017) 33–40.
[30] G. Pozo-Lopez, A.M. Condo, S.P. Limandri, R.H. Mutal, E. Winkler, S.E. Urreta, L. M. Fabietti, Microstructure and magnetic properties of as-cast Ni2MnGa rods and tubes solidified by suction casting, Mater. Charact. 158 (2019), 109956.
[31] L. Pfeuffer, A. Gracia-Condal, T. Gottschall, D. Koch, T. Faske, E. Bruder, J. Lemke, A. Taubel, S. Ener, F. Scheibel, K. Durst, K.P. Skokov, L. Manosa, A. Planes, O. Gutfleisch, Influence of microstructure on the application of Ni-Mn-In Heusler compounds for multicaloric cooling using magnetic field and uniaxial stress, Acta Mater. 217 (2021), 117157.
[32] A. Poulon, S. Brochet, J.C. Glez, J.D. Mithieux, J.B. Vogt, Influence of texture and grain size on martensitic transformations occurring during low-cycle fatigue of a fine-grained austenitic stainless steel, Adv. Eng. Mater. 12 (2010) 1041–1046.
[33] P. Hilkhuijsen, H.J.M. Geijselaers, T.C. Bor, The influence of austenite texture on the martensitic transformation of an austenitic stainless steel, J. Alloy Compd. 577 (2013) S609–S613.
[34] Z. Yang, D.Y. Cong, X.M. Sun, Z.H. Nie, Y.D. Wang, Enhanced cyclability of elastocaloric effect in boron-microalloyed Ni-Mn-In magnetic shape memory alloys, Acta Mater. 127 (2017) 33–42.
[35] G. Cavazzini, F. Cugini, D. Delmonte, G. Trevisi, L. Nasi, S. Ener, D. Koch, L. Righi, M. Solzi, O. Gutfleisch, F. Albertini, Multifunctional Ni-Mn-Ga and Ni-Mn-Cu-Ga Heusler particles towards the nanoscale by ball-milling technique, J. Alloy Compd. 872 (2021), 159747.
[36] Y.H. Qu, D.Y. Cong, X.M. Sun, Z.H. Nie, W.Y. Gui, R.G. Li, Y. Ren, Y.D. Wang, Giant and reversible room-temperature magnetocaloric effect in Ti-doped Ni-Co-Mn-Sn magnetic shape memory alloys, Acta Mater. 134 (2017) 236–248.
[37] O. Gutfleisch, T. Gottschall, M. Fries, D. Benke, I. Radulov, K.P. Skokov, H. Wende, M. Gruner, M. Acet, P. Entel, M. Farle, Mastering hysteresis in magnetocaloric materials, Philos T R Soc A 374 (2016), 20150308.
[38] C. Zimm, A. Jastrab, A. Sternberg, V. Pecharsky, K. Gschneidner, M. Osborne, I. Anderson, Description and performance of a near-room temperature magnetic refrigerator, Adv. Cryog. Eng. 43 (1998) 1759–1766.
[39] Y.H. Qu, D.Y. Cong, S.H. Li, W.Y. Gui, Z.H. Nie, M.H. Zhang, Y. Ren, Y.D. Wang, Simultaneously achieved large reversible elastocaloric and magnetocaloric effects and their coupling in a magnetic shape memory alloy, Acta Mater. 151 (2018) 41–55.
[40] Y.H. Qu, D.Y. Cong, Z. Chen, W.Y. Gui, X.M. Sun, S.H. Li, L. Ma, Y.D. Wang, Large and reversible inverse magnetocaloric effect in Ni48.1Co2.9Mn35.0In14.0 metamagnetic shape memory microwire, Appl. Phys. Lett. 111 (2017), 192412.
[41] J. Liu, Y.Y. Gong, Y.R. You, X.M. You, B.W. Huang, X.F. Miao, G.Z. Xu, F. Xu, E. Brück, Giant reversible magnetocaloric effect in MnNiGe-based materials: minimizing thermal hysteresis via crystallographic compatibility modulation, Acta Mater. 174 (2019) 450–458.
[42] M. Fries, L. Pfeuffer, E. Bruder, T. Gottschall, S. Ener, L.V.S. Diop, T. Grob, K. P. Skokov, O. Gutfleisch, Microstructural and magnetic properties of Mn-Fe-P-Si (Fe2P-type) magnetocaloric compounds, Acta Mater. 132 (2017) 222–229.
[43] B. Kaeswurm, V. Franco, K.P. Skokov, O. Gutfleisch, Assessment of the magnetocaloric effect in La,Pr(Fe,Si) under cycling, J. Magn. Magn. Mater. 406 (2016) 259–265.
[44] L. Huang, D.Y. Cong, L. Ma, Z.H. Nie, Z.L. Wang, H.L. Suo, Y. Ren, Y.D. Wang, Large reversible magnetocaloric effect in a Ni-Co-Mn-In magnetic shape memory alloy, Appl. Phys. Lett. 108 (2016), 032405.
[45] Z.B. Li, J.J. Yang, D. Li, Z.Z. Li, B. Yang, H.L. Yan, C.F. Sanchez-Valdes, J.L. S. Llamazares, Y.D. Zhang, C. Esling, X. Zhao, L. Zuo, Tuning the reversible magnetocaloric effect in Ni-Mn-In-based alloys through Co and Cu co-doping, Adv. Electron Mater. 5 (2019), 1800845.
[46] F. Guillou, G. Porcari, H. Yibole, N. van Dijk, E. Brück, Taming the first-order transition in giant magnetocaloric materials, Adv. Mater. 26 (2014) 2671–2675.
[47] J.W. Lai, H. Sepehri-Amin, X. Tang, J. Li, Y. Matsushita, T. Ohkubo, A.T. Saito, K. Hono, Reduction of hysteresis in (La1-xCex)y(MnzFe11.4-z)Si1.6 magnetocaloric compounds for cryogenic magnetic refrigeration, Acta Mater. 220 (2021), 117286.
[48] F.Q. Zhang, I. Batashev, N. van Dijk, E. Brück, Effect of off-stoichiometry and Ta doping on Fe-rich (Mn,Fe)2(P,Si) based giant magnetocaloric materials, Scripta Mater. 226 (2023), 115253.
[49] V.A. Chernenko, E. Cesari, J. Pons, C. Segui, Phase transformations in rapidly quenched Ni-Mn-Ga alloys, J. Mater. Res. 15 (2000) 1496–1504.
[50] A. Planes, L. Manosa, E. Vives, Acoustic emission in martensitic transformations, J. Alloy Compd. 577 (2013) S699–S704.
[51] T.Y. Hsu, L.F. Yan, The effect of quenched-in vacancies on the martensitic-transformation, J. Mater. Sci. 18 (1983) 3213–3218.
[52] S.L. Liu, H.C. Xuan, T. Cao, L.B. Wang, Z.G. Xie, X.H. Liang, H. Li, L. Feng, F. H. Chen, P.D. Han, Magnetocaloric and elastocaloric effects in all-d-metal $Ni_{37}Co_9Fe_4Mn_{35}Ti_{15}$ magnetic shape memory alloy, Phys. Status Solidi A 216 (2019), 1900563.
[53] Z.Q. Guan, X.J. Jiang, J.L. Gu, J. Bai, X.Z. Liang, H.L. Yan, Y.D. Zhang, L.D. Esling, X. Zhao, L. Zuo, Large magnetocaloric effect and excellent mechanical properties near room temperature in Ni-Co-Mn-Ti non-textured polycrystalline alloys, Appl. Phys. Lett. 119 (2021), 051904.
[54] S. Samanta, S. Ghosh, S. Chatterjee, K. Mandal, Large magnetocaloric effect and magnetoresistance in Fe-Co doped Ni50-x(FeCo)xMn37Ti13 all-d-metal Heusler alloys, J. Alloy Compd. 910 (2022), 164929.
[55] Z.Q. Guan, J. Bai, Y. Zhang, J.L. Gu, X.J. Jiang, X.Z. Liang, R.K. Huang, Y.D. Zhang, C. Esling, X. Zhao, L. Zuo, Revealing essence of magnetostructural coupling of Ni-Co-Mn-Ti alloys by first-principles calculations and experimental verification, Rare Metals 41 (2022) 1933–1947.
[56] A.N. Khan, L.M. Moreno-Ramirez, A. Diaz-Garcia, J.Y. Law, V. Franco, All-d-metal Ni(Co)-Mn(X)-Ti (X = Fe or Cr) Heusler alloys: enhanced magnetocaloric effect for moderate magnetic fields, J. Alloy Compd. 931 (2023), 167559.
[57] J. Dong, Z.H. Liu, X.D. Si, T. Zhou, J. Lin, Y.S. Liu, Martensitic transformation and magnetocaloric effect of Cr-doped Mn-Ni-Fe-Ti all-d-metal Heusler alloys near room temperature, Solid State Commun. 362 (2023), 115099.
[58] J. Joseph, T. Jarvis, X.H. Wu, N. Stanford, P. Hodgson, D.M. Fabijanic, Comparative study of the microstructures and mechanical properties of direct laser fabricated and arc-melted AlxCoCrFeNi high entropy alloys, Mat. Sci. Eng. A Struct. 633 (2015) 184–193.
[59] E. Karakose, M. Keskin, Effect of solidification rate on the microstructure and microhardness of a melt-spun Al-8Si-1Sb alloy, J. Alloy Compd. 479 (2009) 230–236.
[60] E.J. Lavernia, T.S. Srivatsan, The rapid solidification processing of materials: science, principles, technology, advances, and applications, J. Mater. Sci. 45 (2010) 287–325.
[61] C.C. Ma, K. Liu, X.Q. Han, S. Yang, N. Ye, J.C. Tang, Martensitic transformation and magnetocaloric effect in melt-spun $Mn_{50}Ni_{31.5}Co_{8.5}Ti_{10}$ all-3D-metal alloy ribbons, J. Magn. Magn. Mater. 493 (2020), 165733.
[62] K. Liu, X.Q. Han, K. Yu, C.C. Ma, Z.S. Zhang, Y. Song, S.C. Ma, H. Zeng, C.C. Chen, X.H. Luo, S.U. Rehman, Z.C. Zhong, Magnetic-field-induced metamagnetic reverse martensitic transformation and magnetocaloric effect in all-d-metal $Ni_{36.0}Co_{14.0}Mn_{35.7}Ti_{14.3}$ alloy ribbons, Intermetallics 110 (2019), 106472.
[63] M.W. Grabski, R. Korski, Grain boundaries as sinks for dislocations, Philos. Mag. 22 (1970) 707–715.
[64] K. Hartman, M. Bertoni, J. Serdy, T. Buonassisi, Dislocation density reduction in multicrystalline silicon solar cell material by high temperature annealing, Appl. Phys. Lett. 93 (2008), 122108.
[65] N.B. Jia, Y.D. Xu, R.R. Guo, Y.X. Gu, X. Fu, Y.H. Wang, W.Q. Jie, Investigation of dislocation migration in substrate-grade CdZnTe crystals during post-annealing, J. Cryst. Growth 457 (2017) 343–348.
[66] K. Sato, T. Yoshiie, T. Ishizaki, Q. Xu, Behavior of vacancies near edge dislocations in Ni and alpha-Fe: positron annihilation experiments and rate theory calculations, Phys. Rev. B 75 (2007), 094109.
[67] T.R. Anantharaman, C. Suryanarayana, A decade of quenching from the melt, J. Mater. Sci. 6 (1971) 1111–1135.
[68] D.A. Porter, K.E. Easterling, Phase Transformations in Metals and Alloys, CRC press, 2009.
[69] D. Hull, D.J. Bacon, Introduction to Dislocations, Butterworth-Heinemann, 2001.
[70] X.L. Xu, H. Hou, Y.H. Zhao, F. Liu, Preparation of bulk crystallite alloys by rapid quenching of bulk undercooled melts, Mater. Sci. Tech. Lond. 34 (2018) 79–85.
[71] X. Lu, L.Y. Miao, Y.F. Zhang, Z. Wang, H. Zhang, G.W. Li, J. Liu, First-order phase transition La-Fe-Si bulk materials with small hysteresis by laser powder bed fusion: microstructure and magnetocaloric effect, Scripta Mater. 232 (2023), 115479.
[72] W. Sha, H.K.D.H. Bhadeshia, Modelling of recrystallisation in mechanically alloyed materials, Mat. Sci. Eng. A Struct. 223 (1997) 91–98.
[73] Q. Jiang, Z. Wen, T. Wang, Grain size limit of nanocrystalline materials obtained by annealing glasses, J. Phys. Condens Mat. 13 (2001) 5503–5506.
[74] Y. Yamaguchi, H. Doryo, M. Yuasa, H. Miyamoto, M. Yamanaka, Deformation and recrystallization behavior of super high-purity niobium for SRF cavity, IOP Conf. Ser. Mater. Sci. Eng. 194 (2017), 012029.
[75] F.J. Humphreys, M. Hatherly, Recrystallization and Related Annealing Phenomena, Elsevier, 2012.
[76] B. Zhang, Y.P. Duan, X. Yang, G.J. Ma, T.M. Wang, X.L. Dong, Y.S. Zeng, Tuning magnetic properties based on FeCoNiSi0.4Al0.4 with dual-phase nano-crystal and nano-amorphous microstructure, Intermetallics 117 (2020), 106678.
[77] W. Xu, B. Zhang, X.Y. Li, K. Le, Suppressing atomic diffusion with the Schwarz crystal structure in supersaturated Al-Mg alloys, Science 373 (2021) 683–687.
[78] C. Segui, E. Cesari, Effect of ageing on the structural and magnetic transformations and the related entropy change in a Ni-Co-Mn-Ga ferromagnetic shape memory alloy, Intermetallics 19 (2011) 721–725.
[79] V. Sánchez-Alarcos, J.I. Pérez-Landazábal, V. Recarte, Influence of long-range atomic order on the structural and magnetic properties of Ni-Mn-Ga ferromagnetic shape memory alloys, Mater. Sci. Forum (2011) 85–103.
[80] C. Segui, E. Cesari, Composition and atomic order effects on the structural and magnetic transformations in ferromagnetic Ni-Co-Mn-Ga shape memory alloys, J. Appl. Phys. 111 (2012), 043914.
[81] M. Khan, J. Jung, S.S. Stoyko, A. Mar, A. Quetz, T. Samanta, I. Dubenko, N. Ali, S. Stadler, K.H. Chow, The role of Ni-Mn hybridization on the martensitic phase transitions in Mn-rich Heusler alloys, Appl. Phys. Lett. 100 (2012), 172403.
[82] V.V. Khovaylo, V.V. Rodionova, S.N. Shevyrtalov, V. Novosad, Magnetocaloric effect in "reduced" dimensions: thin films, ribbons, and microwires of Heusler alloys and related compounds, Phys. Status Solidi B 251 (2014) 2104–2113.

[83] A. Fujita, K. Fukamichi, F. Gejima, R. Kainuma, K. Ishida, Magnetic properties and large magnetic-field-induced strains in off-stoichiometric Ni-Mn-Al Heusler alloys, Appl. Phys. Lett. 77 (2000) 3054–3056.
[84] A.K. Nayak, K.G. Suresh, A.K. Nigam, Correlation between reentrant spin glass behavior and the magnetic order-disorder transition of the martensite phase in Ni-Co-Mn-Sb Heusler alloys, J. Phys. Condens Mat. 23 (2011), 416004.
[85] J. Sharma, K.G. Suresh, A. Alam, Large exchange bias in Mn-Ni-Sn Heusler alloys: role of cluster spin glass state, Phys. Rev. B 107 (2023), 054405.
[86] R. Krause-Rehberg, H.S. Leipner, Positron Annihilation in semiconductors: Defect Studies, Springer, 1999.
[87] R.W. Siegel, Positron annihilation spectroscopy, Ann. Rev. Mater. Sci. 10 (1980) 393–425.
[88] F. Tuomisto, I. Makkonen, Defect identification in semiconductors with positron annihilation: experiment and theory, Rev. Mod. Phys. 85 (2013) 1583–1631.
[89] J. Cizek, Characterization of lattice defects in metallic materials by positron annihilation spectroscopy: a review, J. Mater. Sci. Technol. 34 (2018) 577–598.
[90] Z.Y. Wu, T. de Krom, G. Colombi, D. Chaykina, G. van Hattem, H. Schut, M. Dickmann, W. Egger, C. Hugenschmidt, E. Brück, B. Dam, S.W.H. Eijt, Formation of vacancies and metallic-like domains in photochromic rare-earth oxyhydride thin films studied by in-situ illumination positron annihilation spectroscopy, Phys. Rev. Mater. 6 (2022), 065201.
[91] X. Zhang, J. Zhang, H.C. Wang, J. Rogal, H.Y. Li, S.H. Wei, T. Hickel, Defect-characterized phase transition kinetics, Appl. Phys. Rev. 9 (2022), 041311.
[92] C. Yang, J.P. Wharry, Role of point defects in stress-induced martensite transformations in NiTi shape memory alloys: a molecular dynamics study, Phys. Rev. B 105 (2022), 144108.